The Diel Profile of Hydroperoxymethyl Thioformate: Evidence for Surface Deposition and Multiphase Chemistry

Michael P. Vermeuel, Gordon A. Novak, Christopher M. Jernigan, Timothy H. Bertram*

Department of Chemistry, University of Wisconsin, Madison, WI, USA

*Correspondence to: T.H. Bertram

Address: 1101 University Ave, Madison, WI, 53703

Email: timothy.bertram@wisc.edu

Table of Contents

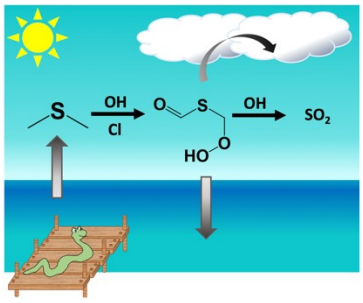

Abstract

Dimethyl sulfide (DMS; CH_3SCH_3), a biogenically produced trace gas emitted from the ocean, accounts for a large fraction of natural sulfur released to the marine atmosphere. The oxidation of DMS in the marine boundary layer (MBL), *via* the hydrogen abstraction pathway, yields the short-lived methylthiomethylperoxy radical (MSP; CH_3SCH_2OO). In the remote MBL, unimolecular isomerization of MSP outpaces bimolecular chemistry leading to the efficient formation of hydroperoxymethyl thioformate (HPMTF; $HOOCH_2SCHO$). Here, we report the first ground observations and diurnal profiles of HPMTF mixing ratios, vertical fluxes and deposition velocities to the ocean surface. Average daytime HPMTF mixing ratios, fluxes, and deposition velocities were recorded at 12.1 pptv, -0.11 pptv m s^{-1}, and 0.75 cm s^{-1}, respectively. The deposition velocity of HPMTF is comparable to other soluble gas phase compounds (e.g., HCOOH and HNO_3), resulting in a deposition lifetime of 30 hours under typical windspeeds (3 m s^{-1}). A box model analysis incorporating the current mechanistic understanding of DMS oxidation chemistry, and geostationary satellite cloud imagery data suggests that the lifetime of HPMTF in the MBL at this sampling location is likely controlled by heterogenous loss to aerosol and uptake to clouds in the morning and evening.

1. Introduction

Emissions of dimethyl sulfide (DMS; CH_3SCH_3) from the oceans provide a significant source of natural reduced sulfur to the marine atmosphere.[1,2] The concerted mechanism of DMS oxidation leads to the formation of sulfur dioxide (SO_2) which can be further oxidized to sulfuric acid

(H_2SO_4), a precursor to new particle formation in the MBL, and methanesulfonic acid (MSA), a contributor to particle growth through condensation. DMS oxidation is initiated through hydroxyl (OH), nitrate (NO_3), bromine oxide (BrO), and chlorine (Cl) radicals, with OH oxidation expected to dominate in the unpolluted marine boundary layer.[3,4] The OH-oxidation of DMS can proceed through either an OH-addition mechanism forming MSA, methanesulfinic acid (MSIA) or dimethylsulfoxide (DMSO), or through a OH abstraction mechanism, previously thought to lead to SO_2 and ultimately sulfate (SO_4^-) production.[5] The fraction of OH addition/abstraction is temperature dependent, with ~70% of OH-initiated oxidation of DMS in the summer MBL proceeding *via* H-abstraction, rapidly producing the methylthiomethyl peroxy radical (MSP; CH_3SCH_2OO) after recombination with atmospheric oxygen (O_2).[3] Until recently, it was assumed that MSP either reacts with the hydroperoxyl radical (HO_2) to terminate as CH_3SCH_2OOH, recombine with another peroxy radical (RO_2) or react with nitric oxide (NO) to largely produce methyl thioformate (MTF; CH_3SCHO) or the radical CH_3SCH_2O, the latter of which terminates as H_2SO_4 or MSA.

Theoretical studies have focused on the chemical fate of MSP in the pristine marine atmosphere where NO, RO_2, and HO_2 are low (<10 pptv),[6,7] and bimolecular removal of MSP is slow.[8,9] Quantum mechanical and kinetic calculations presented by Wu, et al. proposed a fast intramolecular H-shift of MSP ($k_{H\text{-}shift,1}$ = 2.1 s^{-1} at 293 K), followed by combination with O_2 to form $MSPO_2$. $MSPO_2$ then undergoes a second H-shift ($k_{H\text{-}shift,2}$= 150 s^{-1} at 293 K) and a recycling of OH to produce hydroperoxymethyl thioformate (HPMTF; $HOOCH_2SCHO$), a hydroperoxyenal.[9] The existence of this product was validated in a laboratory study, with the authors also suggesting a MSP autoxidation rate as limited by the first H-shift ($k_{H\text{-}shift,1}$=0.23 s^{-1} at

293 K).[8] As of now, it is assumed that HPMTF is mainly removed through OH-oxidation at a relatively slow rate ($k_{HPMTF+OH}$ = 1.4 x 10^{-12} cm^3 $molecules^{-1}$ s^{-1}) as determined through the Wu et al. computational study. Most recently, HPMTF was observed in a global airborne study (the NASA atmospheric tomography study; ATom) with observed concentration ratios of DMS:HPMTF regularly at 1:1 during the day, demonstrating HPMTF as a major reservoir for marine sulfur.[4] In the ATom study it was also noted that HPMTF is strongly anti-correlated with observed clouds, proposing fast removal of HPMTF by cloud uptake.

Here we present observations of HPMTF mixing ratios ([HPMTF]; pptv), vertical fluxes (F_{HPMTF}; pptv m s^{-1}) and deposition velocities (v_d(HPMTF) = *F(HPMTF)*/[HPMTF]; cm s^{-1}) at a coastal site in La Jolla, CA in the summer of 2018 as part of a study measuring the air-sea exchange of trace gases at the ocean surface.[10] The observed diel profile in HPMTF is evaluated with a 0-D box model that incorporates meteorological and chemical constraints from onsite measurements and assimilated products, estimated rates of heterogenous uptake to aerosol particles, and the most current understanding of the chemical rates that control production and loss of HPMTF. Our model results suggest that the current recommendation for $k_{HPMTF+OH}$ is too slow and a rate constant closer to the experimentally-determined OH-oxidation of MTF, which is structurally similar to HPMTF, better matches our observations (k_{MTF+OH}=1.1 x 10^{-11} cm^3 $molecules^{-1}$ s^{-1}).[11] To validate the role of cloud uptake in the lifetime of HPMTF ($\tau_{HPMTF} = \frac{[HPMTF]}{L_{HPMTF}}$, where L_{HPMTF} is the HPMTF loss rate) remote sensing imagery from the Geostationary Operational Environmental Satellite-16 (GOES-16) was used to calculate cloud fractions over the La Jolla area. This analysis reveals a consistent diel profile in cloud fraction, due to stratocumulus clearings common to the eastern Pacific, that drives the observed diel profile in HPMTF. Through this analysis we propose that

heterogenous loss to aerosol particles and uptake to clouds play an important role in controlling the lifetime of HPMTF at this coastal site in the morning and evening and are important mechanisms to be considered in future models that include DMS oxidative chemistry.

2. Materials and Methods

2.1 CIMS Detection of HPMTF. Continuous measurements of HPMTF were made with a chemical ionization time of flight mass spectrometer (CI-ToFMS, TOFWERK Inc. and Aerodyne Research Inc.) utilizing iodide (I^-) reagent ion chemistry.[12] A complete description of this instrument can be found in Bertram et al. 2011.[13] Chemical ionization mass spectrometry (CIMS) employing I^- chemistry has been used to quantify a wide number of oxidized organic and inorganic compounds, as well as halogen species, at high sensitivities.[14–16] The HPMTF product ion is detected as the adduct $I{\cdot}HOOCH_2SCHO^-$ and quantified at unit mass -m/*Q* 235 (where -m/Q is negative mass to charge ratio). Potential compounds isobaric with HPMTF and the process to filter those contaminant peaks are presented in the Supporting Information (SI). Determination of the calibration factor of HPMTF was performed after the study period by way of a contained flow tube experiment that generated OH radicals in the presence of DMS. A sensitivity of 1.17 ncps $pptv^{-1}$ was determined for an $I{\cdot}H_2O^-$: I^- of 0.63. Due to constant heating of the inlet and IMR, the experimental $I{\cdot}H_2O^-$: I^- was kept close to 0.63 ± 0.02 More details on the experiment for determining the sensitivity and its water dependence is presented in the SI (Figures S1-S2).[11,17–19]

2.2 Concentration and Vertical Flux Measurements at Scripps Pier. The summer 2018 flux study performed at the Ellen Browning Scripps Memorial Pier (referred to herein as Scripps Pier) is described extensively in Novak, et al. 2020,[10] but relevant details are outlined here. Scripps Pier

136 is a coastal Pacific site located in La Jolla, CA that has been previously used for flux studies of
137 trace gases (N_2O_5, SO_2), marking its suitability for observations of air-sea exchange.[20,21] The CI-
138 ToFMS employed I^- chemistry from July 24-August 03 2018 while deployed to the 330-m pier,
139 13-m above the mean lower tide level. Ambient air was sampled through a 20-m perfluroralkoxy
140 alkane (PFA) inlet manifold consisting of a sample line, an overflow line for zeroing, and a
141 calibration line for standard additions while held at a constant temperature of 40°C. When
142 quantifying the signal of HPMTF it is assumed no HPMTF is lost to the inlet, although it is possible
143 that an inlet this long could introduce irreversible wall partitioning effects. The inlet manifold was
144 mounted on a 6.1 m long boom and collocated with a Gil-Sonic HS-50 sonic anemometer
145 measuring 3-D winds. Data from both the CI-ToFMS and sonic anemometer were saved at a rate
146 of 10 Hz. Ambient air was collected for 30 minutes for calculating flux periods, followed by 2
147 minutes of zeroing with dry N_2 and 3 minutes of a standard addition of isotopically labeled
148 $H^{13}COOH$ by way of dilution of a custom permeation tube. Further detail on this experiment along
149 with figures of merit for HPMTF quantification can be found in the SI (Table S1).[13,22]
150
151 Air-to-sea fluxes of purely depositing compounds (i.e. HPMTF, HCOOH) were processed using
152 the eddy covariance (EC) technique, where flux (F) is calculated as the mean product of the
153 instantaneous variances of the vertical wind velocity (w) and ambient mixing ratios of a particular
154 compound (C) collected during a 30-minute averaging period:
155 $$F_C = \overline{w'C'} \quad \text{(E1).}$$
156 For gases with high effective solubility, transfer across an air-liquid interface can be parameterized
157 as
158 $$F_C = -K_a\left(C_a - \frac{C_w}{K_H}\right) = -k_a(C_a) \quad \text{(E2)}$$

where K_a is the total transfer velocity that represents the limits of exchange across both sides of the air-sea interface from the point of view of the air side, C_w and C_a are the waterside and airside concentrations of compound C, respectively, K_H is the dimensionless Henry's law constant (M atm^{-1}), and k_a is the solubility-independent air-side transfer velocity (cm s^{-1}). [23,24] K_a can be further expressed in terms of the two single-phase transfer velocities, k_a and k_w, the former being the solubility independent water-side transfer velocity:

$$K_a = [\frac{1}{k_a} + \frac{1}{k_w K_H}]^{-1} \quad \text{(E3)}$$

In the high solubility case K_H>>1 and K_a=k_a, which can be parameterized by physical constraints that drive exchange (e.g. diffusivity of molecule in air, surface drag)[25], the airside transfer velocity of a soluble compound is also considered its deposition velocity, (k_a≅v_d when K_H>>1). Exchange velocities (v_{ex}, cm s^{-1}) were determined by dividing the flux by the averaged mixing ratio during a particular flux period:

$$v_{ex} = \frac{F_c}{\bar{C}} \quad \text{(E4).}$$

And v_d is defined as the inverse of v_{ex} (v_d=-v_{ex}). Individual flux periods were filtered based on standard techniques for assessing air parcel sourcing, surface drag, and stationarity. A discussion of EC calculations, quality assessment, and filter techniques can be found in the SI (Table S2; Figures S3-S4).[21,26–31]

2.3 Box Model Analysis. A 0-D box model was built in MATLAB using the Master Chemical Mechanism (MCM) v3.3.1 in the Framework for 0-D Atmospheric Modeling (F0AM) to assess existing HPMTF chemical mechanisms.[18] In the model, we set the MSP autoxidation rate, that produces HPMTF, as the temperature independent first H-shift as presented in Berndt et al. ($k_{H\text{-}shift,1}$ = 0.23).[8] This production rate is used as it is the only published experimentally-observed value

to date and is fast enough to compete with the reaction of MSP and onsite NO. Model solutions using all of the published values of $k_{H\text{-}shift,1}$ are presented in the SI. More details on the reaction scheme and constraints used in the model are presented in the SI (Table S3; Figure S5).[20,32,33]

Meteorological inputs were acquired from the NOAA National Data Buoy Center (Stations LJPC1 and LJAC1) as well as from an onsite temperature and relative humidity data logger (OM-62, Omega Engineering). Chemical constraints included measured [O_3] and [$ClNO_2$], an assumed [OH] profile that followed the solar cycle and peaks at 4.0 x 10^6 molecules cm^{-3}, a constant concentration of DMS (140 pptv) as determined by measurements at the same site in early September 2019, a constant concentration of NO_2 (200 pptv) as determined from onsite measurements (Figure S12), and constant concentrations of other major trace gases as listed in Table S3. Dry deposition of HPMTF is set to 0.75 cm s^{-1} based on results from this study and a static boundary layer height (BLH) of 800 m is used, based on consideration of its distance from the shoreline (SI).[28,34,35] The model runs shown in the main text do not include anthropogenic VOC or NO_3 oxidative reactions due to the large uncertainties the latter creates for coastal [NO_3] that may misrepresent nighttime HPMTF; a decision further explained in 4.1 and the SI.

Uptake of trace gases to marine aerosol particles is treated as heterogenous loss with a unimolecular rate constant of:

$$k_{het} = \frac{\gamma A \bar{c}}{4} \quad \text{(E5)}$$

where γ is the dimensionless uptake coefficient, A is the particle surface area density (μm^2 cm^{-3}), and $\bar{c}$ is the mean molecular speed of the molecule of interest (cm s^{-1}). A constant particle surface area of 150 μm^2 cm^{-3} is used, based on published observations of typical coastal, marine aerosol

particle size distributions.[36–39] A complete table of base case model constraints are found in Table S3 and the sensitivity of HPMTF to select constraints is presented in the SI (Figures S6-S11).[6,7,20,40–42]

3. Results

3.1 Summary of Select Measurements. Figure 1 presents observations of HPMTF at Scripps Pier from July 24 – August 3, 2018. The nighttime contribution of the isobaric compound N_2O_5 to signal at -*m/Q* 235 was removed when $\tau(N_2O_5 + NO_3)$ was longer than 5 min, leaving an HPMTF signal window from 600 – 2100 PDT (Figure S11).[43] The diurnal profile of HPMTF (Fig. 1a) displays a rise after 600 PDT, concurrent with a change in winds from offshore (WD<180°) to onshore (WD≥180°). HPMTF mixing ratios plateau from 1400-1600 PDT before falling to near the detection limit by 2000 PDT. The diurnal profile in HPMTF peaks late in the afternoon before rapidly being removed by sunset. Windspeed and thus DMS emission fluxes also peak in the late afternoon which may partially account for the observed profile.[44] However, the decrease in HPMTF past 1600 PDT cannot be explained by changes in windspeed or wind direction (Figure S12), or by removal through OH oxidation (where $k_{HPMTF+OH}$ is on the order of 10^{-12}-10^{-11} cm^3 $molecules^{-1}$ s^{-1} and $\tau_{HPMTF+OH} \approx 14$ hr)[4,8,9] or deposition to the ocean surface as measured in this study ($\tau_{deposition} \approx 30$ hr).

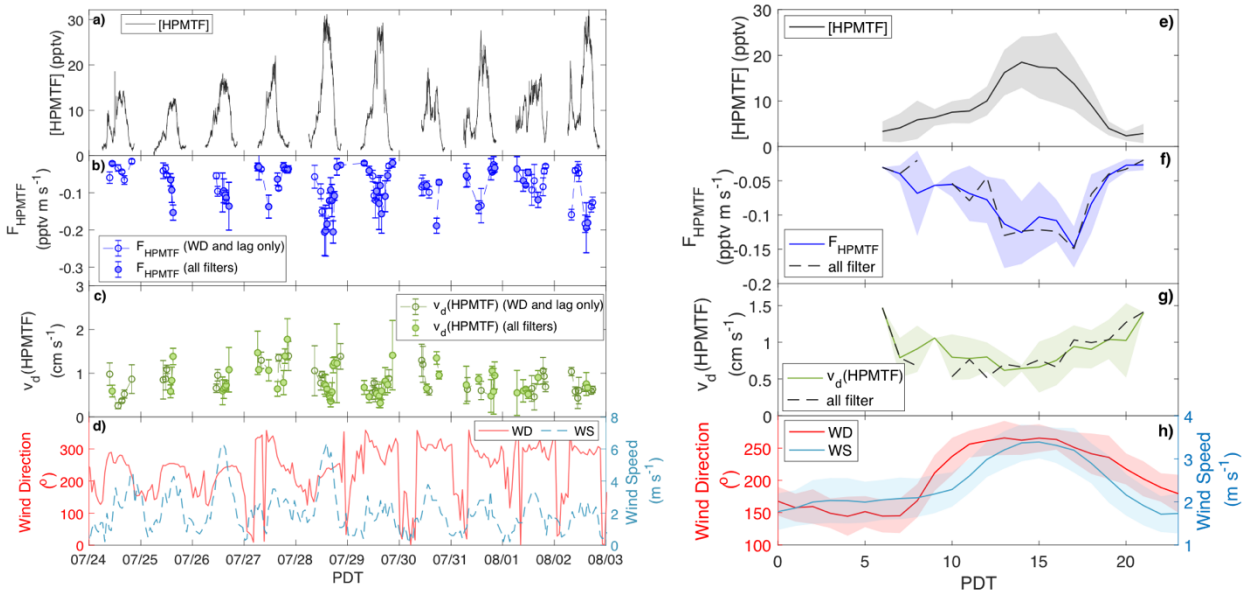

223

224 Figure 1: Time series of a.) mixing ratios b.) fluxes, and c.) deposition velocities of HPMTF along with
225 recorded d.) meteorological wind direction and wind speed. Mixing ratios are presented at a 30-sec
226 resolution. Fluxes and v_d are presented as 30-min averages with errors as explained in the main text. Wind
227 direction and speed are hourly averages. Diurnal averages of e.) mixing ratios, f.) flux, and g.) deposition
228 velocities of HPMTF are also presented along with diurnal averages of h.) wind direction and wind speed.

229 The diurnal profile of F_{HPMTF} (Figure 1f) follows that of [HPMTF] and windspeed, rising
230 throughout the day, coming to a peak near 1400 PDT and plateauing until 1600 PDT before
231 decreasing to the limit of no net surface exchange. The diurnal profile of v_d(HPMTF) is fairly static
232 from 600-2100 PDT, with a daytime (900-1800 PDT) average of 0.75 cm s^{-1}; comparable to that
233 of a highly soluble molecule such as nitric acid (v_d= 0.5-2.0 cm s^{-1}).[45,46] The daily maximum
234 HPMTF deposition flux ranged from 0.07-0.21 pptv m s^{-1} (5.26 $\times 10^8$ molecules cm^{-2} s^{-1}) with
235 daytime v_d(HPMTF) maxima ranging from 0.73-1.7 cm s^{-1}. Temporal profiles of surface horizontal
236 wind at 10-m (U_{10}) were consistent throughout the observation period; offshore winds were
237 sustained until around 700 PDT, on average, switching to onshore winds until the early morning.

238

3.2 Deposition Velocities of HPMTF. The air-side transfer velocity term (k_a) in E2 can be expressed in terms of resistances to deposition

$$k_a^{-1} = r_{turbulence} + r_{diffusion} + r_{surface} \quad \text{(E5)}$$

where $r_{turbulence}$ is the aerodynamic resistance, $r_{diffusion}$ is the resistance posed by diffusivity in air, and $r_{surface}$ is the resistance to air–sea gas transfer arising from physical–chemical interactions on a molecular scale layer at the surface. The resistance to turbulence can be approximated by the momentum transfer velocity (k_{mom}, cm s^{-1}):

$$r_{turbulence}{}^{-1} = k_{mom} = \frac{F_{mom}}{\bar{\rho} U_{10}} \quad \text{(E6)}$$

where F_{mom} is the momentum flux (kg m^{-2} s^{-2}) and $\bar{\rho}$ is the density of air (kg m^{-3}). The momentum flux during this study was calculated through the EC method for the vertical (w) and zonal (u) winds and the meridional (v) and zonal winds:

$$F_{mom} = \bar{\rho}\sqrt{\overline{(w'u')^2} + \overline{(v'u')^2}} \quad \text{(E7).}$$

To better understand the processes controlling the air to sea deposition of HPMTF, we compare the U_{10} dependences of v_d(HPMTF), k_{mom}, and the v_d of the water soluble molecule formic acid (HCOOH; K_H=5600 M atm^{-1})[24,47] also measured in this study (Figure 2). The observed v_d(HPMTF) reaches a maximum of 1.7 cm s^{-1} and above windspeeds of 5 m s^{-1} v_d(HPMTF) no longer exhibits values above 0.7 m s^{-1}. These high windspeed periods were primarily associated with air parcels received from La Jolla Cove (220° > WD ≥ 180°), which may have impacted flow characteristics and biased the measured flux low. Although the data presented in Figure 2a are filtered for coastal influence (WD < 220° were removed), this turnaround at high U_{10} is exhibited at higher

windspeeds in both v_d(HPMTF) for the July observation period and k_{mom}

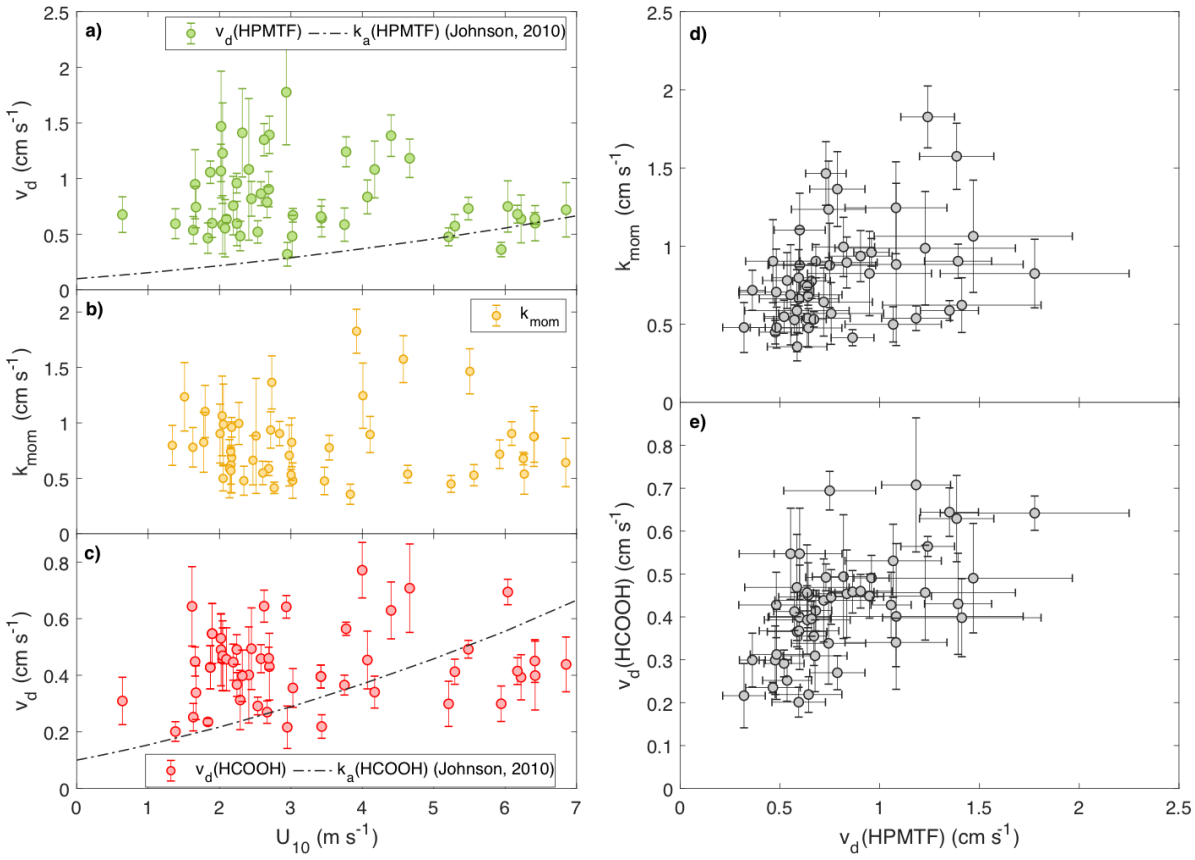

Figure 2: Dependence of a.) v_d(HPTMF), b.) k_{mom}, and c.) v_d(HCOOH) on 10-m windspeed. Calculations of k_a, following the method of Johnson, et al. 2010, are included in panel c for a sea surface temperature of 20°C and an ocean salinity of 35 practical salinity units (PSU).[25] Regressions of d.) k_{mom} and e.) v_d(HCOOH) against v_d(HCOOH) are in good agreement implying fast air-side transfer.

(Fig. 2b), suggesting an increase in $r_{turbulence}$ (E5-6) concurrent with these periods of higher windspeed at this site. Since k_{mom} and v_d are close in scale beyond a U_{10} of 2 m s^{-1}, it is possible that v_d(HPMTF) is mainly limited by $r_{turbulence}$, maintaining a low barrier imposed by solubility (Figure 2b). Included in Figure 2a is the windspeed dependence of parameterized k_a (E2) using the temperature- and salinity-dependent method of Johnson, 2010, where k_a is calculated using a sea-surface temperature of 20°C and ocean salinity (35 PSU).[25]

The v_d(HPMTF) is comparable to v_d(HCOOH) (Fig. 2c), with HCOOH a highly soluble molecule expected to deposit at the airside limit ($v_d(HCOOH)_{max,obs}$ = 0.77 cm s^{-1}). Also included in Figure 2c is the parameterized k_a of HCOOH following the parameterization of Johnson, et al. 2010.[25] There is good agreement between measured v_d(HCOOH) and k_a(HCOOH), suggesting that the measurements fall in line with this numerical scheme and the parameterization can be used to infer a low water-side resistance of HPMTF at this site. Figures 2d and 2e present reasonable agreement of v_d(HPMTF) with k_{mom} (m=0.90; R^2=0.43) and good agreement of $\underline{v_d}$(HCOOH) and v_d(HPMTF) (m=0.48; R^2=0.60). We present the relationship of $\underline{v_d}$(HCOOH) and v_d(HPMTF) to highlight that HPMTF deposition closely resembles another known soluble molecule, HCOOH. However as HCOOH has a comparably high solubility to HPMTF and a lower molecular weight, it is expected that $\underline{v_d}$(HCOOH) would be equal or greater than v_d(HPMTF), with expected $\underline{v_d}$(HCOOH):v_d(HPMTF) on the order of 1:1 and greater rather than the observed 0.48:1. The comparison of these three transfer velocities imply that HPMTF: 1) deposits rapidly to the ocean surface at the air side resistance limit (i.e. limited by $r_{turbulence}$), 2) is very subsaturated in the ocean surface waters, and 3) must have a high solubility (K_H>>1) or fast chemical conversion in ocean surface water. These implications call for the necessity of experimental determinations of K_H to further validate these claims.

4. Discussion

To assess the relevant chemistry and physics that determine the HPMTF diurnal profile, we utilize a 0-D chemical box model that incorporates known gas phase and heterogeneous production and loss processes. The base model framework is described in section 2.3 and the base case parameters are outlined in Table S3. In the discussion that follows, we present model solutions to validate

potential gas phase and heterogeneous loss processes. To incorporate cloud chemistry, we first describe a novel approach for modeling cloud chemistry based on geostationary satellite imagery. We then present the potential role for cloud uptake as an HPMTF loss process. The box model analysis is performed for July 26, 2019, a day that presents a typical HPMTF and regional cloud fraction profile for the study period. Sensitivities of this model to select ambient mixing ratios of key precursors, chemical rate constants, and physical parameters are presented in the SI.

4.1 Potential HPMTF Loss Mechanisms: Oxidation and Heterogenous Uptake. Currently, there are three prior studies of the chemical production and loss of HPMTF, where P_{HPMTF} is limited by a first intramolecular H-shift of MSP, and the reaction rate for the gas-phase reaction of HPMTF with OH has been calculated. As noted previously, Wu et al (2015) calculated $k_{H\text{-}shift,1}$ of 2.1 s^{-1}, Berndt et al. (2019) measured $k_{H\text{-}shift,1}$ of 0.23 s^{-1}, and Veres et al. (2020) calculated $k_{H\text{-}shift,1}$ of 0.041 s^{-1}, all at temperature of around 293 K.[4,8,9] In this analysis we use the Berndt et al. calculation of $k_{H\text{-}shift,1}$, as it is currently the only experimentally-determined value to date. Figure S9 presents model sensitivity to the other $k_{H\text{-}shift,1}$ values along with the concurrent changes in experimental HPMTF calibration factors that would arise from utilizing a different $k_{H\text{-}shift,1}$.

Loss of HPMTF by OH oxidation has only been explored in the computational study by Wu et al., with a $k_{HPMTF+OH}$ of 1.4 x 10^{-12} cm^3 $molecules^{-1}$ s^{-1}. At an upper limit we can expect the rate of oxidative loss of HPMTF to OH to be much slower than that of C5-HPALD, a hydroperoxyenal that is formed from isomerization and decomposition of isoprene hydroperoxyl radicals (ISO_2), the isoprene analogues of MSP. An experimentally-derived $k_{C6\text{-}HPALD+OH}$ was determined to be 5.1 x 10^{-11} cm^3 $molecules^{-1}$ s^{-1} at 296 ± 2 K, serving as an upper bound for model sensitivity to HPMTF

loss to OH, as we expect C5-HPALD to react with OH faster than HPMTF due to the presence of double bonds in C5-HPALD that are absent in HPMTF.[48] The Wu, et al. rate constant for reaction with OH can also be compared to an experimentally-determined rate for the OH-oxidation of MTF, a sulfur-containing molecule structurally similar to HPMTF in that the hydroperoxide group is replaced with a methyl group (k_{MTF+OH} = 1.11 ± 0.22 x 10^{11} cm^3 $molecules^{-1}$ s^{-1} at 298 K).[11].

Figure 3a presents model solutions of HPMTF using rate constants for oxidative removal by OH of either $k_{HPMTF+OH}$ as calculated in Wu et al. (red line), k_{MTF+OH} (green line), or $k_{HPALD+OH}$ (blue line) all in units of cm^3 $molecules^{-1}$ s^{-1}. In this implementation of the model no heterogenous loss is considered, with L_{HPMTF} only driven by chemical loss to OH and dry deposition. From Figure 3a, it is evident that the currently used $k_{HPMTF+OH}$ of 1.4 x 10^{-12} cm^3 $molecules^{-1}$ s^{-1} is likely too slow to replicate observations, with the model solution over a factor of 3 larger than observations at the observed peak in [HPMTF]. Model solutions that use $k_{HPMTF+OH}$=k_{MTF+OH} are a factor of 2 larger than observed peak [HPMTF], also implying that this rate would be too slow if it is assumed that L_{HPMTF} is solely due to gas-phase reactions and dry deposition. When using a $k_{HPMTF+OH}$=$k_{HPALD+OH}$, model [HPMTF] underpredicts the observed peak [HPMTF]. Each of the modeled series in Fig. 3a fail to replicate the shape of the diel profile of observed [HPMTF] which consists of a small peak around 1000 PDT due to Cl-initiated oxidation of DMS, a second peak around 1300 PDT, due to OH-initiated oxidation, and a fast decline from 1600-1800 PDT. This failure to replicate [HMPTF] in the morning and late afternoon implies that τ_{HPMTF} is not solely controlled by gas-phase loss to OH and that another loss route must be present at this site.

Other gas-phase oxidative loss routes of HPMTF that can be considered are loss to O_3 and NO_3. Reactions of O_3 with C6-HPALD indicate that the chemical lifetime of C6-HPALD due to OH is over 200 times shorter than that of C6-HPALD to O_3 (at [OH] = 4 x 10^6 molecules cm^{-3} and [O_3] = 30 ppbv).[48] Due to the presence of a more O_3-reactive carbon-carbon double bond in a C6-HPALD that is absent in HPMTF, it is expected that HPMTF ozonolysis proceeds very slowly, with a lifetime of HPMTF against O_3 more comparable to DMS (148 days).[49] Daytime loss of HPMTF to NO_3 is negligible due to the short photolysis lifetime of NO_3, however it can play a role in nocturnal loss of HPMTF that currently has not been explored. The analysis presented here does not account for nocturnal chemistry of NO_3 that may be important in coastal DMS oxidation chemistry. A final consideration for chemical loss is through photolysis of the aldehyde group. We expect that this pathway is considered to have a small impact on the diel profile of [HPMTF] based on experimentally-determined MTF photolysis lifetime of 3.7 days at the equator and 5.4 days at 40^{o}N [11]. However, there is no experimentally measured HPMTF photolysis rate.

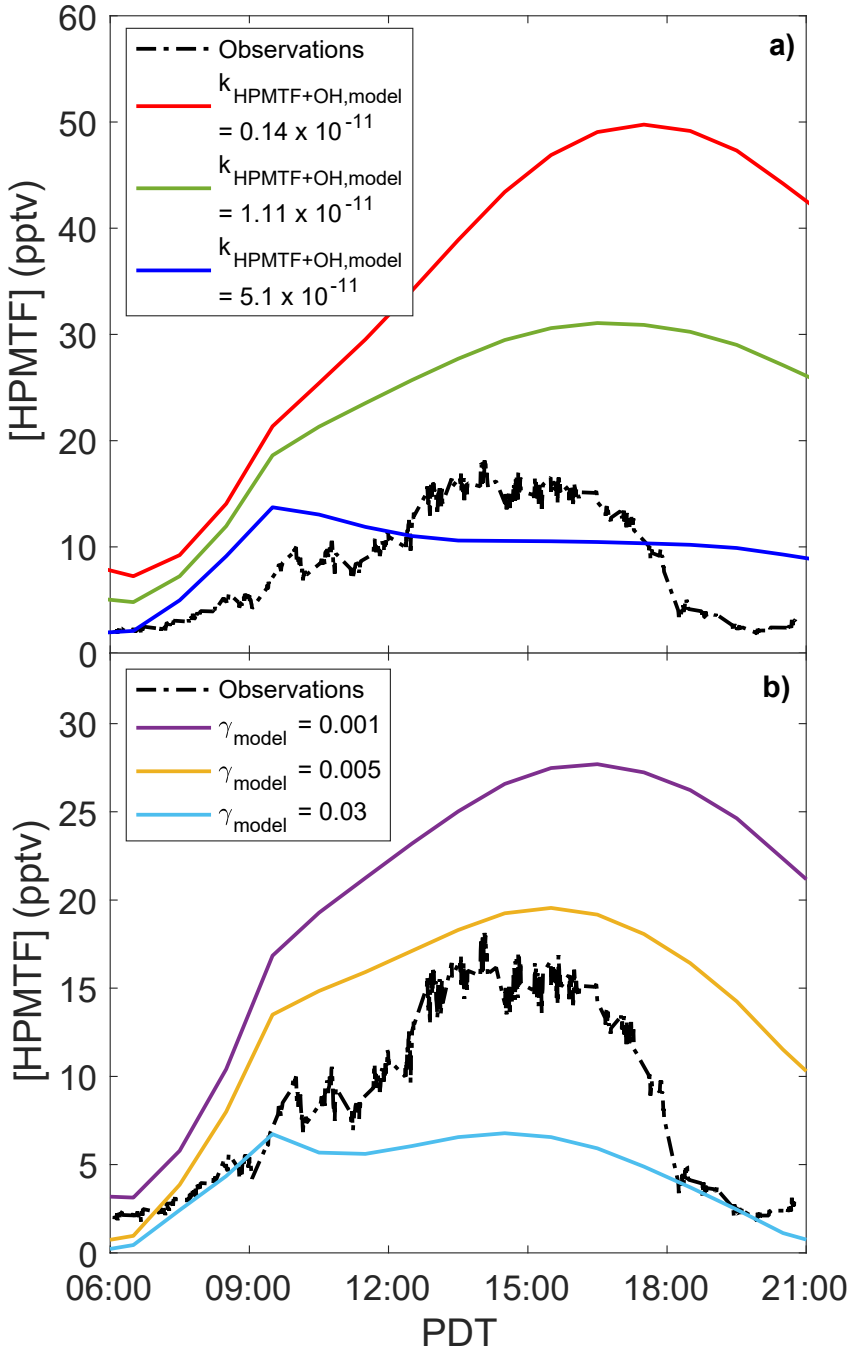

353

354 Figure 3: a.) Box-model simulations of HPMTF as a function of the implemented HPMTF + OH rate
355 constant ($k_{HPMTF+OH}$; cm^3 molecules^{-1} s^{-1}) , where $k_{HPMTF+OH}$ is set equal to: k_{MTF+OH} (green line), $k_{C6\text{-}HPALD+OH}$
356 (blue line), and the Wu, et al. computationally-derived $k_{HPMTF+OH}$ (red line). b.) Box-model simulations of
357 HPMTF as a function of the implemented heterogenous uptake coefficient (γ), where γ ranges from 0.001-
358 0.03 and $k_{HPMTF+OH}$=1.11 x 10^{-11}. Measurements of HPMTF on July 26th, 2018 are shown as black dash-
359 dots.

360

The box-model fails to replicate the diurnal profile and magnitude of HPMTF using only gas-phase loss processes, suggesting an important role of heterogenous or multiphase chemistry. To date, there are no experimental studies of the heterogeneous reactions of HPMTF to constrain the model. To assess the sensitivity of HPMTF to γ_{HPMTF}, we set an upper and lower limit of 0.001 and 0.03 to span a reasonable range of reactive uptake coefficient for comparable molecules. Figure 3b shows the results of these sensitivity runs, with model and measurements best agreeing near γ_{HPMTF} =0.005 at peak [HPMTF]. Based on the implied high solubility and/or ocean surface reactivity from the v_d(HPMTF) measured in this study, it is plausible that γ_{HPMTF} would be within this magnitude for faster uptake. However, this route still cannot explain the apparent short atmospheric lifetime of HPMTF in the morning and late afternoon shown in the observations. In the following section we explore the potential for cloud uptake of HPMTF as a controlling loss mechanism.

4.2 Assessing the Influence of Marine Clouds on HPMTF. Clouds can serve as efficient sinks for water-soluble species that undergo reactions within the cloud droplet. As discussed by Veres et al. (2020), HPMTF mixing ratios were found to be consistently depleted when passing through the cloud layer, suggesting HPMTF may undergo irreversible uptake to cloud droplets.[4] The overall lifetime for cloud processing of species with irreversible uptake in the turbulently mixed boundary layer is controlled by the rate of mixing into the cloud layer and the residence time within the cloud layer.[50] Once a parcel is mixed into the cloud layer, uptake is limited by gas phase diffusion to droplet surfaces, with lifetimes on the order of 5 s for HNO_3 in fair weather cumulus clouds.[51] Holmes et al. have implemented a revised scheme for cloud uptake in a global transport which included cloud spatial information and explicitly treated the mixing rate of parcels into

clouds.[50] In that study, the loss rates of N_2O_5 to clouds was found to be limited by the mixing rate of boundary layer air parcels into clouds, with the lifetime of N_2O_5 within the cloud layer found to be 10 s.

Stratocumulus clouds within the turbulent MBL are a common feature over cooler regions of the subtropical and mid-latitude oceans, where mean annual coverage can exceed 50%.[52] Globally, stratus and stratocumulus clouds are typically present over 10-70% of the MBL, suggesting loss to clouds within the MBL to be a potentially significant term in reactive trace gas budgets. Based on imagery of clouds and surfaces from the geostationary satellite GOES-16[53], we suggest that HPMTF undergoes cloud uptake due to the presence of clouds over coastal southern California.

Imagery from GOES-16 reveals a diurnal pattern in cloud cover over the southern coast of California for the July 24 – August 3, 2018 period. An example of this is shown in Figure 4a, where true color imagery of the contiguous United States (CONUS) cropped to southern California on July 23rd, 2018 is shown. A clear-sky period with cities labeled for regional clarity is shown along with a red box denoting a pixel counting region around the measurement site. Images cropped to the same domain for July 26th at 700, 1400, and 1800 PDT (Fig. 3b-d) were converted from color to gray scale to discriminate between cloud, land, and water based on gray scale value (GV=0-256). Examples of the discernment of land, ocean, and cloud from this analysis are shown in the SI (Figure S14-S15). The imagery in Figure 4b-d shows a clear diel profile in cloud cover, where at 700 PDT (Fig. 4b) there is presence of stratocumulus clouds over Scripps Pier and most of southern CA. By 1400 PDT (Fig. 4c) the clouds have mostly cleared from the measurement site,

and by 1800 PDT (Fig. 4d) the clouds have returned, displaying a diurnal profile that is typical of stratocumulus clearings in the summertime eastern Pacific.[52,54–56]

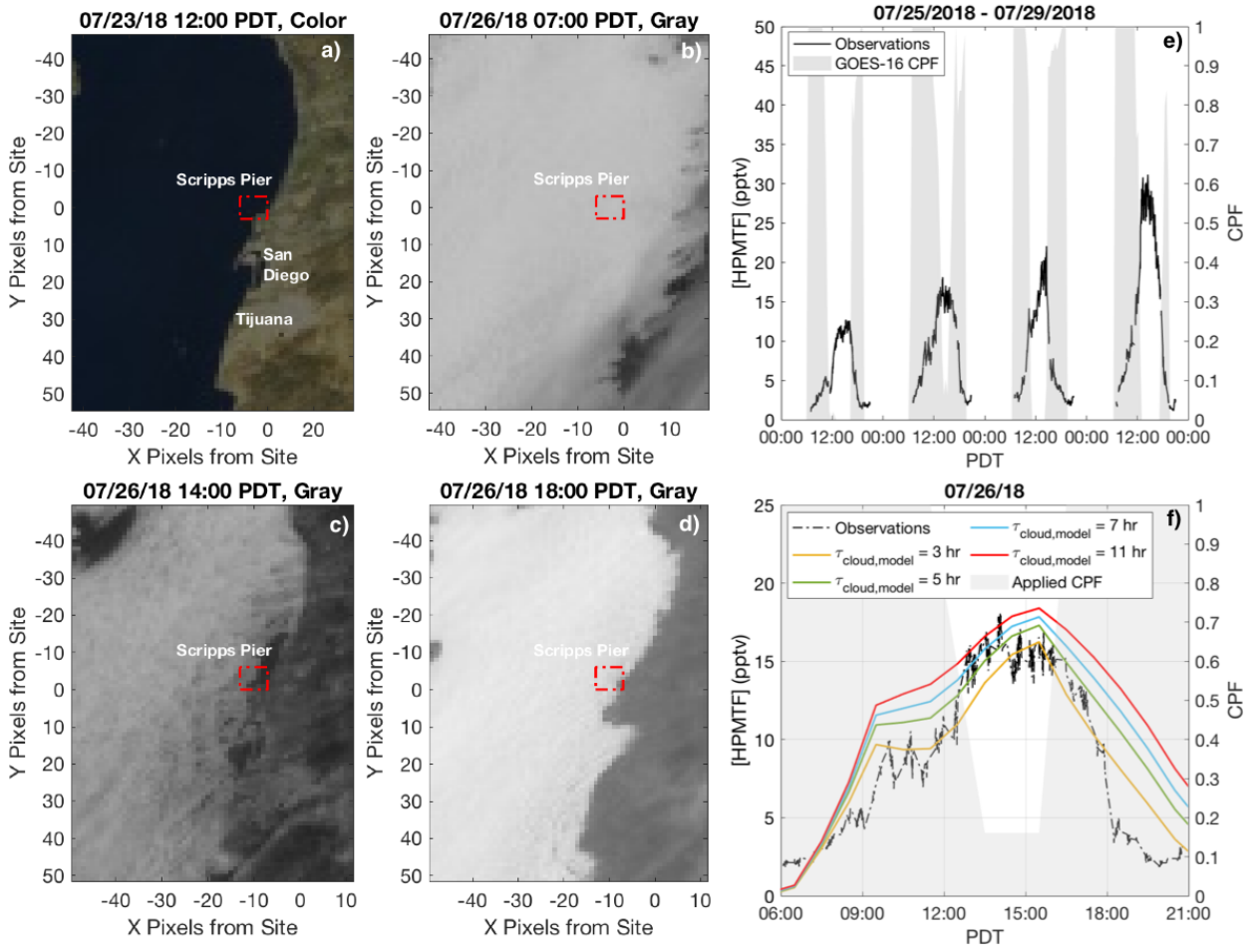

Figure 4: Images from GOES-16 over coastal southern California show varying amounts of cloud cover over Scripps Pier throughout the day. a.) A color reference of a clear sky day on 07/23/18 is presented for clarity. Comparison of grayscale images from b.) 700, c.) 1400, and d.) 1800 PDT on 07/26/18 show cloud cover during the morning and early evening but little cloud cover during the afternoon within a 49 pixel^2 domain (red box). Pixels in this region are ~0.7 km. e.) A time series of the cloud pixel fraction (CPF) within the 49 pixel^2 domain compared to the [HPMTF] time series from July 25-29, 2018 reveals an anticorrelation of [HPMTF] with cloud cover. f.) Box model simulations of 07/26/18 that implement a cloud uptake loss pathway at the timescale of τ_{cloud} show a strong influence of clouds on τ_{HPMTF} in the morning and late afternoon. A modified CPF is applied (grey area) based on domain sensitivity tests (Figure S16).

Pixels were counted within a counting domain for 25-minute averages of imagery and hourly thresholds of GV for clouds (e.g. $GV_{cloud,17PDT} \geq 160$) were used to determine the fraction of clouds in each time point (CPF; cloud pixel fraction). Figure 4e shows CPF for July 25-29, along with

measured [HPMTF] and highlights a clear anticorrelation between [HPMTF] and CPF suggesting the influence of clouds on measured HPMTF. CPFs were used in a box model to assess the impact of cloud uptake on the HPMTF profile by applying a time-dependent cloud uptake lifetime (τ_{cloud}) that is scaled by observed CPF. Figure 4f shows the model solutions using base case constraints and an applied τ_{cloud} from 3-11 hrs. Upon comparison of model to measurements, τ_{cloud} would need to be relatively fast (3-5 hours) to best match the observations. When τ_{cloud} exceeds 7 hours, cloud uptake has minimal effect on HPMTF loss and no longer controls τ_{HPMTF}. Details on GOES-16 imagery, GV cloud thresholding, selection of counting region, and applied CPF profile are presented in the SI (Figure S14-S16). The observed diel profile in HPMTF is reproduced when we apply a time-dependent HPMTF loss to clouds indicating that HPMTF cloud uptake likely dictates τ_{HPMTF} in the cloudy MBL. Future field observations should target HPMTF chemistry in both cloud free and cloudy regions.

4.3 Model Outlook

At this time, accurate chemical modeling of the diel profile in HPMTF is limited by the lack of laboratory constraints on HPMTF loss rates, both in the gas-phase and *via* heterogeneous and multiphase reactions. In this study, τ_{cloud} was not directly measured but rather determined by comparison to chemical observations. Vertical airborne flux measurements of HPMTF in cloudy environments will prove useful for validating this loss pathway. Although this study uses a reliable estimate of aerosol surface at this site, the heterogenous loss of HPMTF to marine aerosol is still a large unknown variable that can drastically modify model solutions within a plausible range of γ_{HPMTF} (Figure 3b) which can then impact other estimations of HPMTF loss processes. Detailed

studies of reactive uptake of HPMTF to aerosol are required to better predict the fate of HPMTF over the ocean surface.

Due to the existence of only a few published HPMTF lab studies, the kinetics involving HPMTF are still prone to uncertainty and require validation through comparison to published studies of analogous molecules. The required constraints on $k_{H\text{-}shift,1}$ and $k_{HPMTF+OH}$ utilized in this case study bring two major implications. The first is that the isomerization of MSP may be slow enough that bimolecular reactions of MSP in coastal regions, where RO_2 and NO have the potential to be sufficiently high enough, may limit the production of HPMTF. The second implication is that loss through OH may be faster than recently published rates, leading to an additional route for overprediction of HPMTF. The ambient observations presented in this analysis may prove useful in the future model evaluations of HPMTF production and loss processes as determined in laboratory studies.

Acknowledgements

This work was supported by National Science Foundation (NSF) Grant GEO AGS 1829667. The authors thank the staff at Scripps Pier, Scripps Institute of Oceanography. Glenn M. Wolfe is gratefully acknowledged for publicly providing the MATLAB based FluxToolbox of analysis scripts as well as the F0AM box model, portions of which were altered for use in this analysis. Code for FluxToolBox and F0AM is archived at https://github.com/AirChem. This research was performed using the computing resources and assistance of the UW-Madison Center for High Throughput Computing (CHTC) in the Department of Computer Sciences. The CHTC is supported by UW-Madison, the Advanced Computing Initiative, the Wisconsin Alumni Research

Foundation, the Wisconsin Institutes for Discovery, and the National Science Foundation, and is an active member of the Open Science Grid, which is supported by the National Science Foundation and the U.S. Department of Energy's Office of Science.

Supporting Information

Extended experimental methods, model descriptions, model runs, and methods for utilizing geostationary satellite imagery. Tables S1-S3 and Figures S1-S16.

References

(1) Andreae, M. O.; Ferek, R. J.; Bermond, F.; Byrd, K. P.; Engstrom, R. .; Hardin, S.; Houmerf, P. D.; LeMarrec, F.; Raemdonck, H. Dimethyl Sulfide in the Marine Atmosphere. *J. Geophys. Res.* **1985**, *90* (D7), 12891–12900. https://doi.org/10.1029/JD090iD07p12891.

(2) Dacey, J. W. H.; Blough, N. V. Hydroxide Decomposition of Dimethylsulfoniopropionate to Form Dimethylsulfide. *Geophys. Res. Lett.* **1987**, *14* (12), 1246–1249.

(3) Barnes, I.; Hjorth, J.; Mihalapoulos, N. Dimethyl Sulfide and Dimethyl Sulfoxide and Their Oxidation in the Atmosphere. *Chem. Rev.* **2006**, *106* (3), 940–975. https://doi.org/10.1021/cr020529+.

(4) Veres, P. R.; Neuman, J. A.; Bertram, T. H.; Assaf, E.; Wolfe, G. M.; Williamson, C. J.; Weinzierl, B.; Tilmes, S.; Thompson, C. R.; Thames, A. B.; et al. Global Airborne Sampling Reveals a Previously Unobserved Dimethyl Sulfide Oxidation Mechanism in the Marine Atmosphere. *Proc. Natl. Acad. Sci.* **2020**, 201919344. https://doi.org/10.1073/pnas.1919344117.

(5) Hoffmann, E. H.; Tilgner, A.; Schrödner, R.; Bräuer, P.; Wolke, R.; Herrmann, H. An Advanced Modeling Study on the Impacts and Atmospheric Implications of Multiphase Dimethyl Sulfide Chemistry. *Proc. Natl. Acad. Sci.* **2016**, *113* (42), 11776–11781. https://doi.org/10.1073/pnas.1606320113.

(6) Vaughan, S.; Ingham, T.; Whalley, L. K.; Stone, D.; Evans, M. J.; Read, K. A.; Lee, J. D.; Moller, S. J.; Carpenter, L. J.; Lewis, A. C.; et al. Seasonal Observations of OH and HO2in the Remote Tropical Marine Boundary Layer. *Atmos. Chem. Phys.* **2012**, *12* (4), 2149–2172. https://doi.org/10.5194/acp-12-2149-2012.

(7) Creasey, D. J.; Evans, G. E.; Heard, D. E.; Lee, J. D. Measurements of OH and HO2 Concentrations in the Southern Ocean Marine Boundary Layer. *J. Geophys. Res. D Atmos.* **2003**, *108* (15), 1–12. https://doi.org/10.1029/2002jd003206.

(8) Berndt, T.; Scholz, W.; Mentler, B.; Fischer, L.; Hoffmann, E. H.; Tilgner, A.; Hyttinen, N.; Prisle, N. L.; Hansel, A.; Herrmann, H. Fast Peroxy Radical Isomerization and OH Recycling in the Reaction of OH Radicals with Dimethyl Sulfide. *J. Phys. Chem. Lett.* **2019**, *10* (21), 6478–6483. https://doi.org/10.1021/acs.jpclett.9b02567.

(9) Wu, R.; Wang, S.; Wang, L. New Mechanism for the Atmospheric Oxidation of Dimethyl Sulfide. The Importance of Intramolecular Hydrogen Shift in a CH3SCH2OO Radical. *J. Phys. Chem. A* **2015**, *119* (1), 112–117. https://doi.org/10.1021/jp511616j.

(10) Novak, G. A.; Vermeuel, M. P.; Bertram, T. H. Simultaneous Detection of Ozone and Nitrogen Dioxide by Oxygen Anion Chemical Ionization Mass Spectrometry : A Fast-Time-Response Sensor Suitable for Eddy Covariance Measurements. *Atmos. Meas. Tech.* **2020**, *1*, 1887–1907.

(11) Patroescu, I. V.; Barnes, I.; Becker, K. H. FTIR Kinetic and Mechanistic Study of the

Atmospheric Chemistry of Methyl Thiolformate. *J. Phys. Chem.* **1996**, *100* (43), 17207–17217. https://doi.org/10.1021/jp961452u.

(12) Huey, L. G.; Hanson, D. R.; Howard, C. J. Reactions of SF6- and I- with Atmospheric Trace Gases. *J. Phys. Chem.* **1995**, *99* (14), 5001–5008. https://doi.org/10.1021/j100014a021.

(13) Bertram, T. H.; Kimmel, J. R.; Crisp, T. a.; Ryder, O. S.; Yatavelli, R. L. N.; Thornton, J. a.; Cubison, M. J.; Gonin, M.; Worsnop, D. R. A Field-Deployable, Chemical Ionization Time-of-Flight Mass Spectrometer. *Atmos. Meas. Tech.* **2011**, *4* (7), 1471–1479. https://doi.org/10.5194/amt-4-1471-2011.

(14) Lee, B. H.; Lopez-hilfiker, F. D.; Mohr, C.; Kurten, T.; Worsnop, D. R.; Joel, A. An Iodide-Adduct High-Resolution Time-of-Flight Chemical- Ionization Mass Spectrometer: Application to Atmospheric Inorganic and Organic Compounds. *Environ.Sci. Technol.* **2014**, *48*, 6309–6317. https://doi.org/10.1021/es500362a.

(15) Lopez-Hilfiker, F. D.; Iyer, S.; Mohr, C.; Lee, B. H.; D'ambro, E. L.; Kurtén, T.; Thornton, J. A. Constraining the Sensitivity of Iodide Adduct Chemical Ionization Mass Spectrometry to Multifunctional Organic Molecules Using the Collision Limit and Thermodynamic Stability of Iodide Ion Adducts. *Atmos. Meas. Tech.* **2016**, *9* (4), 1505–1512. https://doi.org/10.5194/amt-9-1505-2016.

(16) Iyer, S.; Lopez-Hilfiker, F.; Lee, B. H.; Thornton, J. a; Kurtén, T. Modeling the Detection of Organic and Inorganic Compounds Using Iodide-Based Chemical Ionization. *J. Phys. Chem. A* **2016**. https://doi.org/10.1021/acs.jpca.5b09837.

(17) Alam, M. S.; Rickard, A. R.; Camredon, M.; Wyche, K. P.; Carr, T.; Hornsby, K. E.; Monks, P. S.; Bloss, W. J. Radical Product Yields from the Ozonolysis of Short Chain

Alkenes under Atmospheric Boundary Layer Conditions. *J. Phys. Chem. A* **2013**, *117* (47), 12468–12483. https://doi.org/10.1021/jp408745h.

(18) Wolfe, G. M.; Marvin, M. R.; Roberts, S. J.; Travis, K. R.; Liao, J. The Framework for 0-D Atmospheric Modeling (F0AM) v3.1. *Geosci. Model Dev.* **2016**, *9* (9), 3309–3319. https://doi.org/10.5194/gmd-9-3309-2016.

(19) Brus, D.; Škrabalová, L.; Herrmann, E.; Olenius, T.; Trávničková, T.; Makkonen, U.; Merikanto, J. Temperature-Dependent Diffusion of H2SO4 in Air at Atmospherically Relevant Conditions: Laboratory Measurements Using Laminar Flow Technique. *Atmosphere (Basel).* **2017**, *8* (7), 1–15. https://doi.org/10.3390/atmos8070132.

(20) Kim, M. J.; Farmer, D. K.; Bertram, T. H. A Controlling Role for the Air-Sea Interface in the Chemical Processing of Reactive Nitrogen in the Coastal Marine Boundary Layer. *Proc. Natl. Acad. Sci. U. S. A.* **2014**, *111* (11), 3943–3948. https://doi.org/10.1073/pnas.1318694111.

(21) Porter, J. G.; De Bruyn, W.; Saltzman, E. S. Eddy Flux Measurements of Sulfur Dioxide Deposition to the Sea Surface. *Atmos. Chem. Phys.* **2018**, *18* (20), 15291–15305. https://doi.org/10.5194/acp-18-15291-2018.

(22) Vermeuel, M. P.; Novak, G. A.; Alwe, H. D.; Hughes, D. D.; Kaleel, R.; Dickens, A. F.; Kenski, D.; Czarnetzki, A. C.; Stone, E. A.; Stanier, C. O.; et al. Sensitivity of Ozone Production to NOx and VOC Along the Lake Michigan Coastline. *J. Geophys. Res. Atmos.* **2019**. https://doi.org/10.1029/2019JD030842.

(23) Liss, P. S.; Slater, P. G. Flux of Gases across the Air-Sea Interface. *Nature* **1974**, *247*, 181–184. https://doi.org/10.1038/247181a0.

(24) Sander, R. Compilation of Henry's Law Constants (Version 4.0) for Water as Solvent.

559 *Atmos. Chem. Phys.* **2015**, *15* (8), 4399–4981. https://doi.org/10.5194/acp-15-4399-2015.
560 (25) Johnson, M. T. A Numerical Scheme to Calculate Temperature and Salinity Dependent
561 Air-Water Transfer Velocities for Any Gas. *Ocean Sci.* **2010**, *6* (4), 913–932.
562 https://doi.org/10.5194/os-6-913-2010.
563 (26) Wilczak, J. M.; Oncley, S. P.; Stage, S. A. Sonic Anemometer Tilt Correction Algorithms.
564 *Boundary-Layer Meteorol.* **2001**, *99* (1), 127–150.
565 https://doi.org/10.1023/A:1018966204465.
566 (27) Foken, T.; Wichura, B. Tools for Quality Assessment of Surface-Based Flux
567 Measurements. *Agric. For. Meteorol.* **1996**, *78* (1–2), 83–105.
568 https://doi.org/10.1016/0168-1923(95)02248-1.
569 (28) Stull, R. B. *An Introduction to Boundary Layer Meteorology*; 1988.
570 (29) Kaimal, J. C. J.; Wyngaard, J. C. J.; Izumi, Y.; Coté, O. R.; Cote, O. R. Spectral
571 Characteristics of Surface-Layer Turbulence. *Q. J. ...* **1972**, *98* (417), 563–589.
572 https://doi.org/10.1002/qj.49709841707.
573 (30) Massman, W. J. The Attenuation of Concentration Fluctuations in Turbulent Flow through
574 a Tube. *J. Geophys. Res.* **1991**, *96* (D8), 15269. https://doi.org/10.1029/91jd01514.
575 (31) Spirig, C.; Neftel, A.; Ammann, C.; Dommen, J.; Grabmer, W.; Thielmann, A.; Schaub,
576 A.; Beauchamp, J.; Wisthaler, A.; Hansel, A. Eddy Covariance Flux Measurements of
577 Biogenic VOCs during ECHO 2003 Using Proton Transfer Reaction Mass Spectrometry.
578 *Atmos. Chem. Phys.* **2005**, *5* (2), 465–481. https://doi.org/10.5194/acp-5-465-2005.
579 (32) Riedel, T. P.; Wolfe, G. M.; Danas, K. T.; Gilman, J. B.; Kuster, W. C.; Bon, D. M.;
580 Vlasenko, A.; Williams, E. J.; Lerner, B. M.; Veres, P. R.; et al. An Mcm Modeling Study
581 of Nitryl Chloride (ClNO2) Impacts on Oxidation, Ozone Production and Nitrogen Oxide

582 Partitioning in Polluted Continental Outflow. *Atmos. Chem. Phys.* **2014**, *14* (8), 3789–
583 3800. https://doi.org/10.5194/acp-14-3789-2014.
584 (33) Mitchell, K. E. The Multi-Institution North American Land Data Assimilation System
585 (NLDAS): Utilizing Multiple GCIP Products and Partners in a Continental Distributed
586 Hydrological Modeling System. *J. Geophys. Res.* **2004**, *109* (D7), D07S90.
587 https://doi.org/10.1029/2003JD003823.
588 (34) Wei, J.; Tang, G.; Zhu, X.; Wang, L.; Liu, Z.; Cheng, M.; Münkel, C.; Li, X.; Wang, Y.
589 Thermal Internal Boundary Layer and Its Effects on Air Pollutants during Summer in a
590 Coastal City in North China. *J. Environ. Sci. (China)* **2018**, *70*, 37–44.
591 https://doi.org/10.1016/j.jes.2017.11.006.
592 (35) Faloona, I.; Lenschow, D. H.; Campos, T.; Stevens, B.; van Zanten, M.; Blomquist, B.;
593 Thornton, D.; Bandy, A.; Gerber, H. Observations of Entrainment in Eastern Pacific
594 Marine Stratocumulus Using Three Conserved Scalars. *J. Atmos. Sci.* **2005**, *62* (9), 3268–
595 3285. https://doi.org/10.1175/JAS3541.1.
596 (36) Ryder, O. S.; Ault, A. P.; Cahill, J. F.; Guasco, T. L.; Riedel, T. P.; Cuadra-Rodriguez, L.
597 A.; Gaston, C. J.; Fitzgerald, E.; Lee, C.; Prather, K. A.; et al. On the Role of Particle
598 Inorganic Mixing State in the Reactive Uptake of N2O5 to Ambient Aerosol Particles.
599 *Environ. Sci. Technol.* **2014**, *48* (3), 1618–1627. https://doi.org/10.1021/es4042622.
600 (37) Modini, R. L.; Frossard, A. A.; Ahlm, L.; Russel, L. M.; Corrigan, C. E.; Roberts, G. C.;
601 Hawkins, L. N.; Schroder, J. C.; Bertram, A. K.; Zhao, R.; et al. Primary Marine Aerosol-
602 Cloud Interactions off the Coast of California. *J. Geophys. Res.* **2015**, *120* (2006), 1751–
603 1762. https://doi.org/10.1002/2014JD022963.Received.
604 (38) Collins, D. B.; Ault, A. P.; Moffet, R. C.; Ruppel, M. J.; Cuadra-Rodriguez, L. A.;

Guasco, T. L.; Corrigan, C. E.; Pedler, B. E.; Azam, F.; Aluwihare, L. I.; et al. Impact of Marine Biogeochemistry on the Chemical Mixing State and Cloud Forming Ability of Nascent Sea Spray Aerosol. *J. Geophys. Res. Atmos.* **2013**, *118* (15), 8553–8565. https://doi.org/10.1002/jgrd.50598.

(39) Riedel, T. P.; Bertram, T. H.; Ryder, O. S.; Liu, S.; Day, D. A.; Russell, L. M.; Gaston, C. J.; Prather, K. A.; Thornton, J. A. Direct N2O5 Reactivity Measurements at a Polluted Coastal Site. *Atmos. Chem. Phys.* **2012**, *12* (6), 2959–2968. https://doi.org/10.5194/acp-12-2959-2012.

(40) Marandino, C. A.; De Bruyn, W. J.; Miller, S. D.; Saltzman, E. S. Open Ocean DMS Air/Sea Fluxes over the Eastern South Pacific Ocean. *Atmos. Chem. Phys.* **2009**, *9* (2), 345–356. https://doi.org/10.5194/acp-9-345-2009.

(41) Dusanter, S.; Vimal, D.; Stevens, P. S.; Volkamer, R.; Molina, L. T. Measurements of OH and HO2 Concentrations during the MCMA-2006 Field Campaign - Part 1: Deployment of the Indiana University Laser-Induced Fluorescence Instrument. *Atmos. Chem. Phys.* **2009**, *9* (5), 1665–1685. https://doi.org/10.5194/acp-9-1665-2009.

(42) Dusanter, S.; Vimal, D.; Stevens, P. S.; Volkamer, R.; Molina, L. T.; Baker, A.; Meinardi, S.; Blake, D.; Sheehy, P.; Merten, A.; et al. Measurements of OH and HO2 Concentrations during the MCMA-2006 Field Campaign - Part 2: Model Comparison and Radical Budget. *Atmos. Chem. Phys.* **2009**, *9* (18), 6655–6675. https://doi.org/10.5194/acp-9-6655-2009.

(43) Brown, S. S.; Stark, H.; Ravishankara, A. R. Applicability of the Steady State Approximation to the Interpretation of Atmospheric Observations of NO3 and N2O5. *J. Geophys. Res. D Atmos.* **2003**, *108* (17), 1–10. https://doi.org/10.1029/2003jd003407.

(44) McGillis, W. R.; Dacey, J. W. H.; Frew, N. M.; Bock, E. J.; Nelson, R. K. Water-Air Flux of Dimethylsulfide. *J. Geophys. Res. Ocean.* **2000**, *105* (C1), 1187–1193. https://doi.org/10.1029/1999jc900243.

(45) Thompson, A. M.; Zafiriou, O. C. Air-Sea Fluxes of Transient Atmospheric Species. *J. Geophys. Res.* **1983**, *88* (C11), 6696–6708. https://doi.org/10.1029/JC088iC11p06696.

(46) Valigura, R. A. Iterative Bulk Exchange Model for Estimating Air-Water Transfer of HNO3. *J. Geophys. Res.* **1995**, *100* (D12), 45–50. https://doi.org/10.1029/95jd03005.

(47) Winiwarter, W.; Fierlinger, H.; Puxbaum, H.; Facchini, M. C.; Arends, B. G.; Fuzzi, S.; Schell, D.; Kaminski, U.; Pahl, S.; Schneider, T.; et al. Henry's Law and the Behavior of Weak Acids and Bases in Fog and Cloud. *J. Atmos. Chem.* **1994**, *19* (1–2), 173–188. https://doi.org/10.1007/BF00696588.

(48) Wolfe, G. M.; Crounse, J. D.; Parrish, J. D.; St. Clair, J. M.; Beaver, M. R.; Paulot, F.; Yoon, T. P.; Wennberg, P. O.; Keutsch, F. N. Photolysis, OH Reactivity and Ozone Reactivity of a Proxy for Isoprene-Derived Hydroperoxyenals (HPALDs). *Phys. Chem. Chem. Phys.* **2012**, *14* (20), 7276–7286. https://doi.org/10.1039/c2cp40388a.

(49) Du, L.; Xu, Y.; Ge, M.; Jia, L.; Yao, L.; Wang, W. Rate Constant of the Gas Phase Reaction of Dimethyl Sulfide (CH3SCH3) with Ozone. *Chem. Phys. Lett.* **2007**, *436* (1–3), 36–40. https://doi.org/10.1016/j.cplett.2007.01.025.

(50) Holmes, C. D.; Bertram, T. H.; Confer, K. L.; Graham, K. A.; Ronan, A. C.; Wirks, C. K.; Shah, V. The Role of Clouds in the Tropospheric NOx Cycle: A New Modeling Approach for Cloud Chemistry and Its Global Implications. *Geophys. Res. Lett.* **2019**, *46* (9), 4980–4990. https://doi.org/10.1029/2019GL081990.

(51) Levine, S. Z.; Schwartz, S. E. In-Cloud and below-Cloud Scavenging of Nitric Acid

Vapor. *Atmos. Environ.* **1982**, *16* (7), 1725–1734. https://doi.org/10.1016/0004-6981(82)90266-9.

(52) Wood, R. Stratocumulus Clouds. *Mon. Weather Rev.* **2012**, *140* (8), 2373–2423. https://doi.org/10.1175/MWR-D-11-00121.1.

(53) Goodman, S. J.; Blakeslee, R. J.; Koshak, W. J.; Mach, D.; Bailey, J.; Buechler, D.; Carey, L.; Schultz, C.; Bateman, M.; McCaul, E.; et al. The GOES-R Geostationary Lightning Mapper (GLM). *Atmos. Res.* **2013**, *125–126*, 34–49. https://doi.org/10.1016/j.atmosres.2013.01.006.

(54) Bretherton, C. S.; Uttal, T.; Fairall, C. W.; Yuter, S. E.; Weller, R. A.; Baumgardner, D.; Comstock, K.; Wood, R.; Raga, G. B. The EPIC 2001 Stratocumulus Study. *Bull. Am. Meteorol. Soc.* **2004**, *85* (7), 967–977. https://doi.org/10.1175/BAMS-85-7-967.

(55) Hignett, P. Observations of Diurnal Variation in a Cloud-Capped Marine Boundary Layer. *Journal of the Atmospheric Sciences*. 1991, pp 1474–1482. https://doi.org/10.1175/1520-0469(1991)048<1474:OODVIA>2.0.CO;2.

(56) Dadashazar, H.; Crosbie, E.; Majdi, M. S.; Panahi, M.; Moghaddam, M. A.; Behrangi, A.; Brunke, M.; Zeng, X.; Jonsson, H. H.; Sorooshian, A. Stratocumulus Cloud Clearings: Statistics from Satellites, Reanalysis Models, and Airborne Measurements. *Atmos. Chem. Phys.* **2020**, *20* (8), 4637–4665. https://doi.org/10.5194/acp-20-4637-2020.